Journal of
Materials Chemistry C

Supporting Information for:

Optical markers of magnetic phase transition in CrSBr

W. M. Linhart,*[a] M.Rybak,[a] M. Birowska,[a] P. Scharoch,[a] K. Mosina,[c] V. Mazanek,[c], D. Kaczorowski,[d] Z. Sofer,[c] and R. Kudrawiec[a]

1 CrSBr synthesis and structural characterisation

Bulk single crystal CrSBr was prepared using a chemical vapour transport method. Chromium, sulphur and bromine elements with a stoichiometry of 1:1:1 were added and sealed in a quartz tube under high vacuum and then placed in a two-zone tube furnace. The material was pre-reacted in an ampoule at 700 °C for 10 hours, and the source and growth ends were kept at 850 and 900 °C, respectively. After 25 h, the temperature gradient was reversed and the hot end gradually increased from 880 to 950 °C in 5 days period. The high-quality CrSBr single crystals were removed from the ampule in an Ar glovebox.

CrSBr exhibits an A-type antiferromagnetic order, with robust FM within the layers, and AFM arrangement of adjacent layers (see Fig. S1).

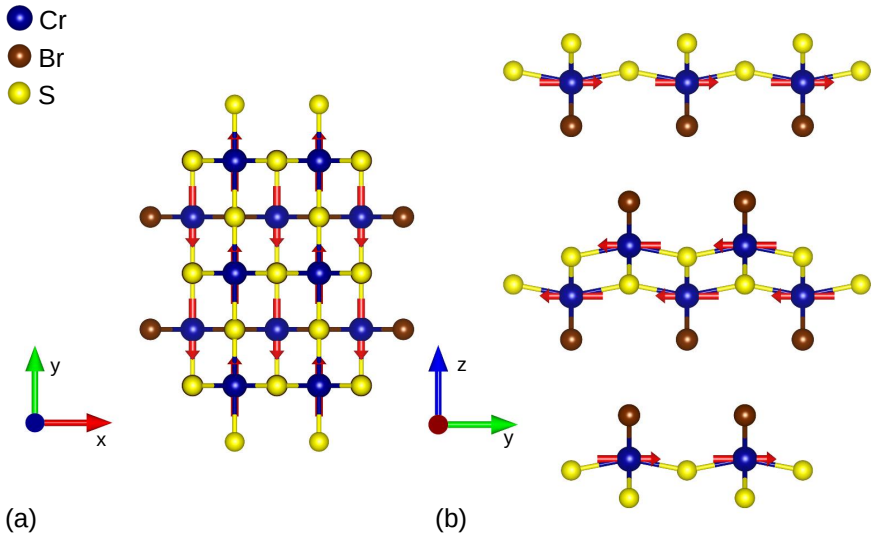

Fig. S1 (Color online) Different crystal orientations for CrSBr. The (a)[001], (b) [100] directions are pointing out of the page for the space group *Pmmn*. The magnetic ground state of the CrSBr bulk system (A-AFM) is marked by red arrows. FM alignment of Cr spins within the layer and AFM alignment of Cr spins in adjacent layers. In panel (b) the layered structure can be clearly seen and the van der Waals gaps between these layers can be distinguished.

The bulk crystal of CrSBr was characterised using XRD (see Fig. S2). Powder XRD data were collected at room temperature on a Bruker D8 Discoverer powder diffractometer (Bruker, Germany) with Parafocusing Bragg-Brentano geometry using CuK_α radiation (λ=0.15418 nm, U = 40 kV, I = 40 mA). The diffraction patterns were collected at room temperature for 2θ values from 5-90°.

[a] *Department of Semiconductor Materials Engineering, Faculty of Fundamental Problems of Technology, Wrocław University of Science and Technology, Wybrzeże Wyspiańskiego 27, 50-370 Wrocław, Poland*
[b] *Institute of Theoretical Physics, Faculty of Physics, University of Warsaw, Pasteura 5, 02-093 Warsaw, Poland*
[c] *Department of Inorganic Chemistry, University of Chemistry and Technology Prague, Technická 5, 166 28 Prague 6, Czech Republic*
[d] *Institute of Low Temperature and Structure Research, Polish Academy of Sciences, ul. Okólna 2, 50-422 Wrocław, Poland*
∗ Corresponding author: wojciech.linhart@pwr.edu.pl

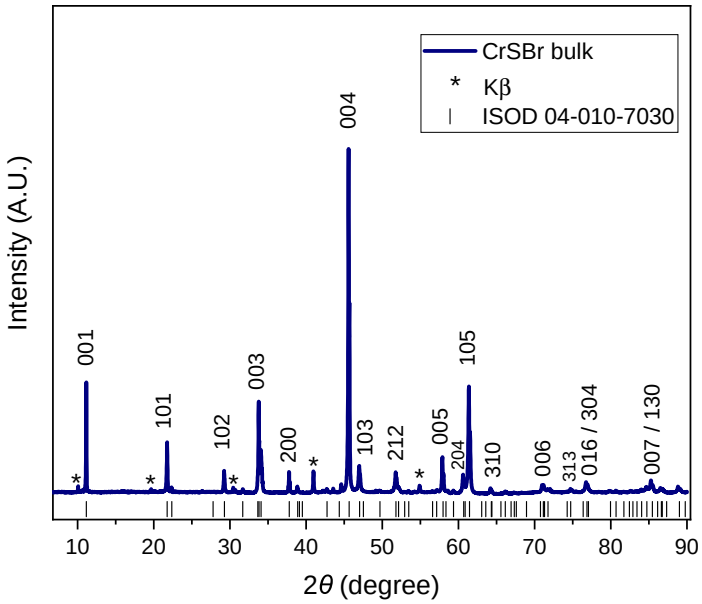

Fig. S2 (Color online) The XRD pattern of the bulk CrSBr material with high crystallinity displayed sharp diffraction peaks and confirmed a successful synthesis of CrSBr without contamination (PDF 04-010-7030). Kβ peaks are labelled with an asterisk.

The acquired data were analysed using HighScore Plus 3.0 software. XRD reveals a pure single-phase CrSBr with a high preferential orientation because of the layered van der Waals structure.

High resolution transmission electron microscopy (HR-TEM) was performed using an EFTEM Jeol 2200 FS microscope (Jeol, Japan). A 200 keV acceleration voltage was used for measurement. Elemental maps and EDS spectra were acquired with SDD detector X-MaxN 80 TS from Oxford Instruments (England). The sample preparation was achieved by drop casting the suspension (1 mg ml^{-1} in acetonitrile) on a TEM grid (Cu; 200 mesh; Formvar/carbon) and dried at 60 °C. The morphology was also investigated using scanning electron microscopy (SEM) with a FEG electron source (Tescan Lyra dual beam microscope). The sample was placed directly on carbon tape and measurements were carried out using a 10 kV electron beam. TEM and SEM results are presented in Figure S3.

High-resolution X-ray photoelectron spectroscopy (XPS) was performed using an ESCAProbeP spectrometer (Omicron Nanotechnology Ltd, Germany) with a monochromatic aluminium X-ray radiation source (1486.7 eV). Wide-scan surveys of all elements were performed, with subsequent high-resolution scans (Fig. S4). The samples were placed on a conductive carrier made from a high-purity silver bar. An electron gun was used to eliminate sample charging during measurement (1-5 V).

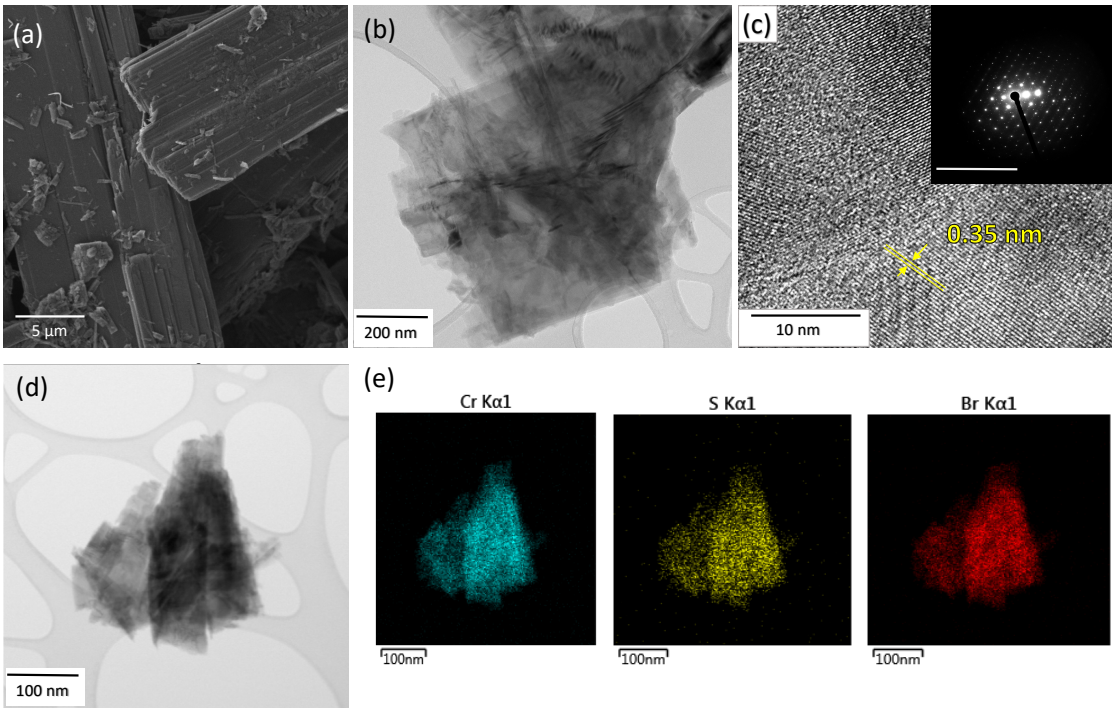

Fig. S3 (Color online) Morphology and microstructure of CrSBr: (a) Scanning electron micrograph of the bulk. (b,d) TEM image of multilayered CrSBr. (c) High-resolution TEM (HR-TEM) image of (b) sheet surface profile and selected area electron diffraction (SAED), shown in inset with a scale 1/0.04 nm. Yellow mark shows lattice fringes with a d-spacing of 0.35±0.03 nm. (e) Elemental mapping images of Cr, Br, S.

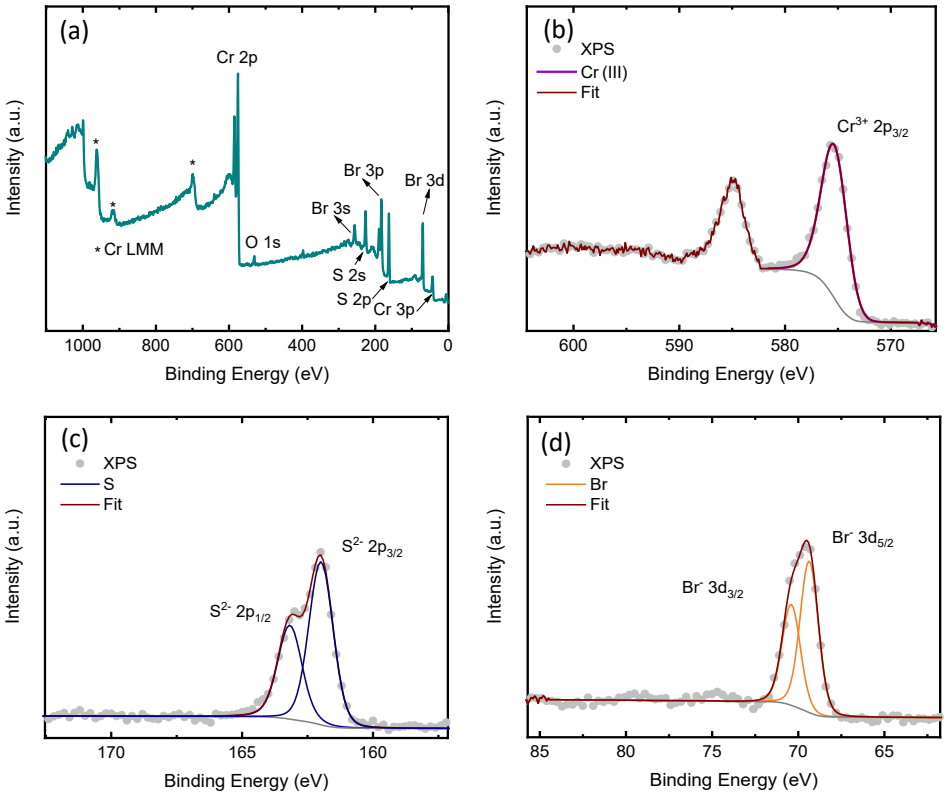

Fig. S4 (Color online) XPS survey spectrum of the spattered sample (a) and high-resolution spectra of the (b) Cr 2p (c) S 2p and (d) Br 3d states of CrSBr,

2 Magnetic Properties

Magnetic properties were investigated in the temperature range of 1.73-300 K and in magnetic fields up to 7 T using a Quantum Design MPMS-XL superconducting quantum interference device (SQUID) magnetometer. Measurements were made on a single crystalline specimen of CrSBr with a magnetic field (H) orientated along the crystallographic direction [001].

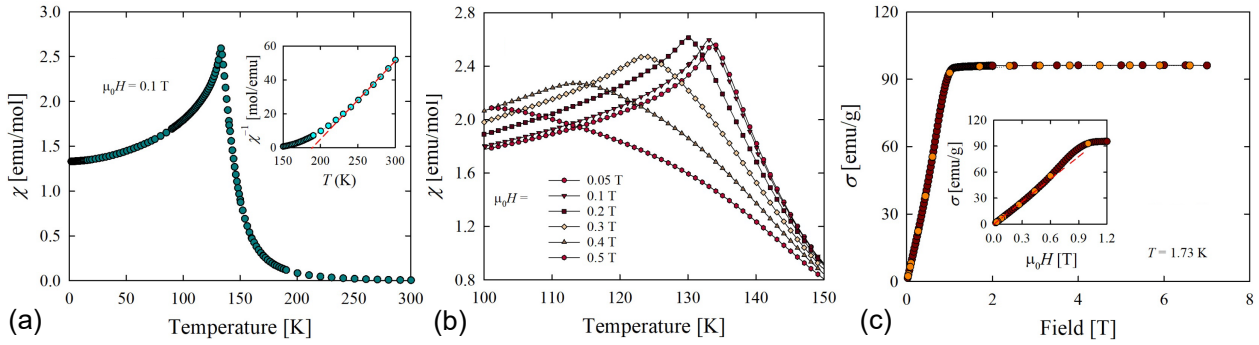

Fig. S5 (Color online) (a) Temperature variation of the molar magnetic susceptibility of single-crystalline CrSBr measured in a magnetic field of 0.1 T applied along the crystallographic c-axis after cooling the sample in a zero field. The inset shows the temperature dependence of the reciprocal magnetic susceptibility. The dashed straight line represents the Curie-Weiss law. (b) Temperature variations of the molar magnetic susceptibility of single-crystalline CrSBr measured as in panel (a) in various external magnetic fields in the vicinity of the AFM phase transition. (c) Magnetic field dependences of magnetisation in single crystalline CrSBr measured at 1.73 K magnetic field applied along the crystallographic c-axis. The dark and light symbols represent the data taken with an increasing and decreasing field, respectively. The inset presents the same magnetisation data in small magnetic fields. The dashed line emphasises the initial straight-line behaviour.

As shown in Fig. S5(a), the temperature dependence of the magnetic susceptibility (χ) of CrSBr exhibits a pronounced maximum at T = 132(1) K that identifies the Néel temperature, in conjunction with data from the literature[1–3]. Above about 240 K, $\chi(T)$ follows a Curie-Weiss law (see the inset of Fig. S5(a)) with the effective magnetic moment μ_{eff} = 4.14(5) μB and the paramagnetic Curie temperature θ_p = 189(3) K. Both parameters are similar to those previously reported for the H $\|c$-axis[2]. The experimental value of μ_{eff} is somewhat larger than the effective magnetic moment predicted for a free Cr^{3+} ion with spin-only momentum S = 3/2 (3.87 μ_B). The large positive value of θ_p reflects strong ferromagnetic interactions in the plane a-b of the CrSBr crystallographic unit cell[1–3]. Below 240 K, χ^{-1}(T) deviates from a straight-line behaviour, probably due to a crystalline electric field.

In the antiferromagnetic region (AFM), magnetic susceptibility decreases smoothly with decreasing temperature down to 1.73 K, in contrast to data in the literature that indicated an additional anomaly near 35 K of unknown origin[2,3]. The latter feature led to a ferromagnetic bifurcation of the $\chi(T)$ curves taken after cooling the specimen in a zero and finite magnetic field, regardless of its direction with respect to the crystal axes[3]. Remarkably, no such effect was found for the CrSBr crystals investigated in this work, thus proving the purely AFM character of their electronic ground state.

Another clue to the AFM ordering in CrSBr came from the measurements of $\chi(T)$ in various magnetic fields, the results of which are shown in Fig. S5(b). With increasing field strength, the susceptibility maximum systematically shifts toward a lower temperature and broadens, in a manner characteristic of antiferromagnets. As can be inferred from the figure, in a magnetic field of 0.4 T, $\chi(T)$ forms an extended maximum near 112 K, but in $\mu_0 H$ = 0.5 T, $\chi(T)$ remains featureless down to 100 K.

The latter finding suggests the occurrence of an order-order magnetic phase transition below 0.5 T, which was observed in the magnetisation (σ) data measured as a function of the magnetic field. As can be seen in the inset of Fig. **??**(c), at T = 1.73 K, σ is initially a linear function of H; however, near 0.45 K, the $\sigma(H)$ isotherm shows an inflection typical for a metamagnetic change in the spin structure. Another anomaly in the isotherm $\sigma(H)$, in the form of a sharp kink, occurs near the critical field $\mu_0 H_c$ = 0.9 T. The latter feature can be attributed to the formation of a field-forced ferromagnetic alignment of all spins along the direction of the magnetic field. The magnitude of H_c is very similar to the value reported in the literature for the H$\|c$-axis[2,3]. In strong magnetic fields, the magnetisation saturates at a value of 96(1) emu/g that corresponds to the magnetic moment μ_{sat} = 2.82(2) μB that is fairly close to the theoretical value of a free Cr^{3+} ion (3 μB). As shown in Fig. S5(c), the $\sigma(H)$ isotherm measured at T = 1.73 K does not exhibit a hysteresis effect, corroborating the AFM nature of the magnetic ordering in the bulk CrSBr crystals investigated.

3 Photoreflectance

Figure S6 shows temperature-dependent PR for the E_3 transition of CrSBr.

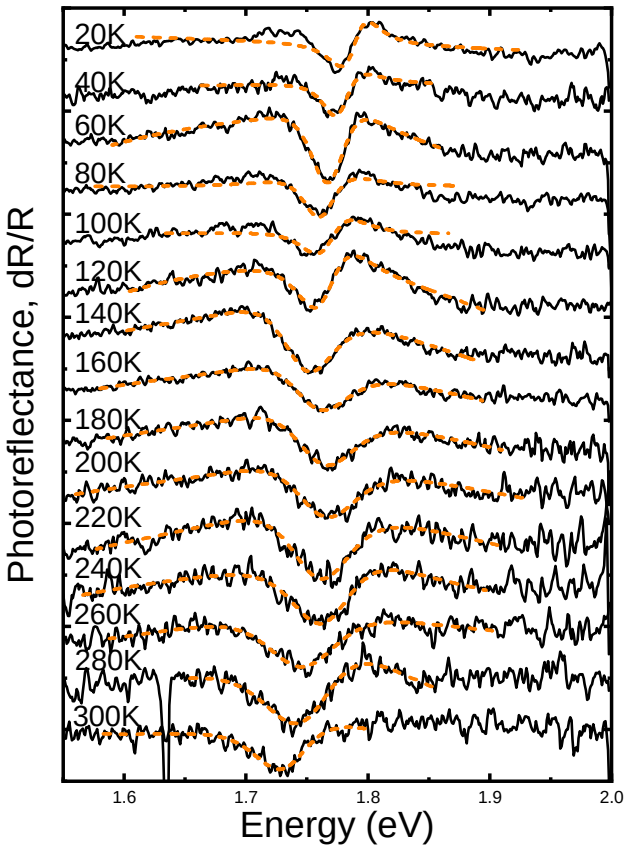

Fig. S6 (Color online) Temperature dependence of the photoreflectance spectra of the E_3 transition with Aspnes fits (dashed lines) of CrSBr.

4 DFT calculations

Figure S7 shows matrix elements in the Brillouin zone, which denote the probabilities of optical transitions. By comparison with the experimental results, we can conclude that the optical transitions occur in the Γ–Z path, where the smallest direct energy gap is observed in the DFT results. We assign the transition between the first valence band (VB_1) and the first conduction band (CB_1) to the resonance E_1 in the PR spectrum. This transition takes place between the Γ and the Z point, where the bands are flat; therefore, it has rather a nesting-like character. Additionally, according to DFT, such a transition is possible because the matrix element in the Γ–Z region has a non-zero value. Figure S8 presents the comparison of the DFT+U calculation for U = 3 eV and U = 5 eV. No significant differences are observed close to the band gap; therefore, for the analysis the model with U = 3 eV was used. In both cases, the band gap was found to be 0.82 eV. Figure S9 shows the band structure calculated with the hybrid functional HSE06 for bulk CrSBr. In this case, the band gap was found to be 1.85 eV, but the energy differences of E_2 and E_1, and E_3 and E_1 are similar to those determined in the framework of DFT+U.

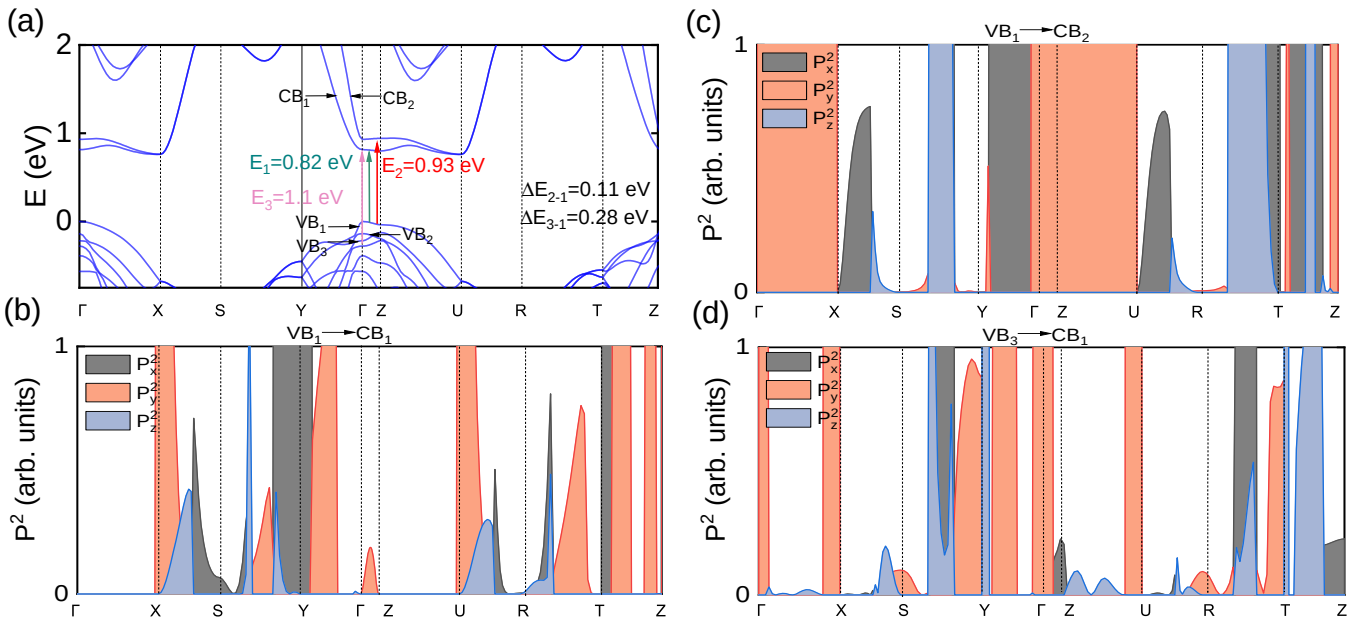

Fig. S7 (Color online) Bandstruture for the magnetic ground state (A-AFM) in the vicinity of Fermi level along high-symmetry lines. Three optically active transitions are denoted by the green (VB_1 to CB_1 at the middle of the Γ-Z line), red (VB_1 to CB_2 at Z k-point), and pink (VB_3 to CB_1 at the Γ k-point). Note that these transitions exhibit non-zero oscillator strength along the "y" direction. The oscillator strength of the three particular transitions along high-symmetry lines in the first BZ: (c) VB_1 to CB_2, (d)VB_1 to CB_1, and (e) VB_3 to CB_1 are presented.

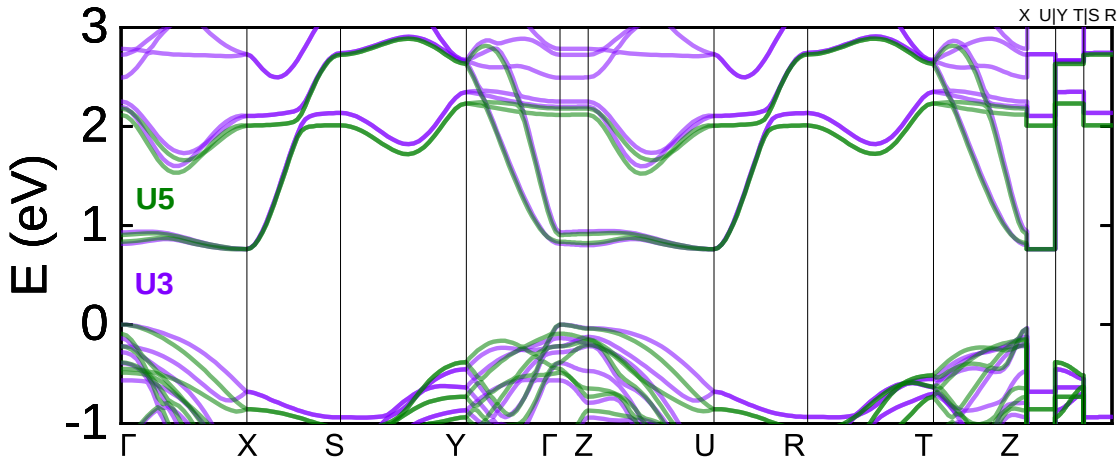

Fig. S8 (Color online) Comparison of the calculated band structures of CrSBr within the DFT + U framework, employing U = 3 eV (violet line) and U = 5 eV (green line).

The splitting band dependency on the overall magnetisation in the CrSBr system is shown in Fig. S10.

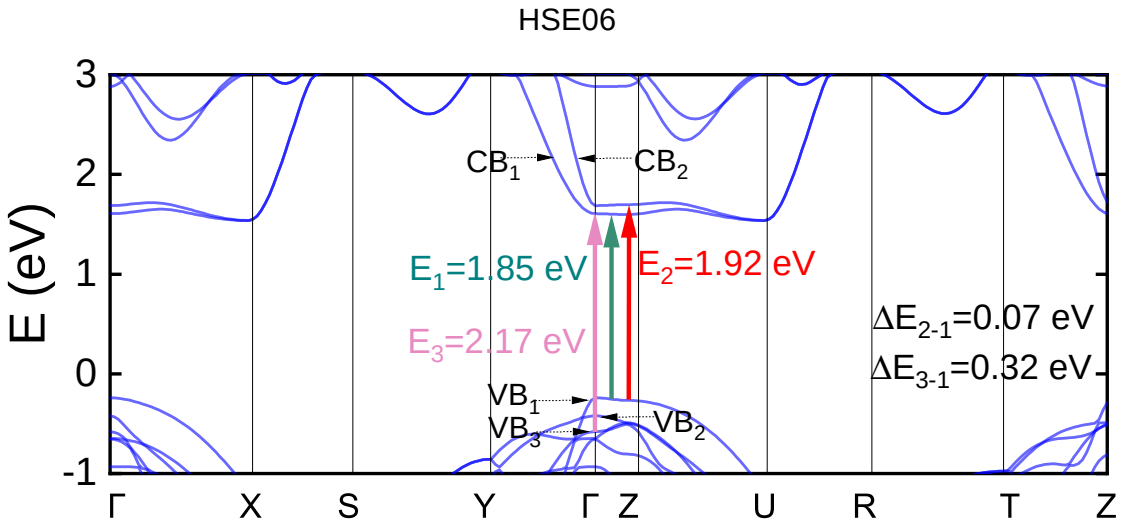

Fig. S9 (Color online) The band structure of CrSBr was calculated using the hybrid functional HSE06.

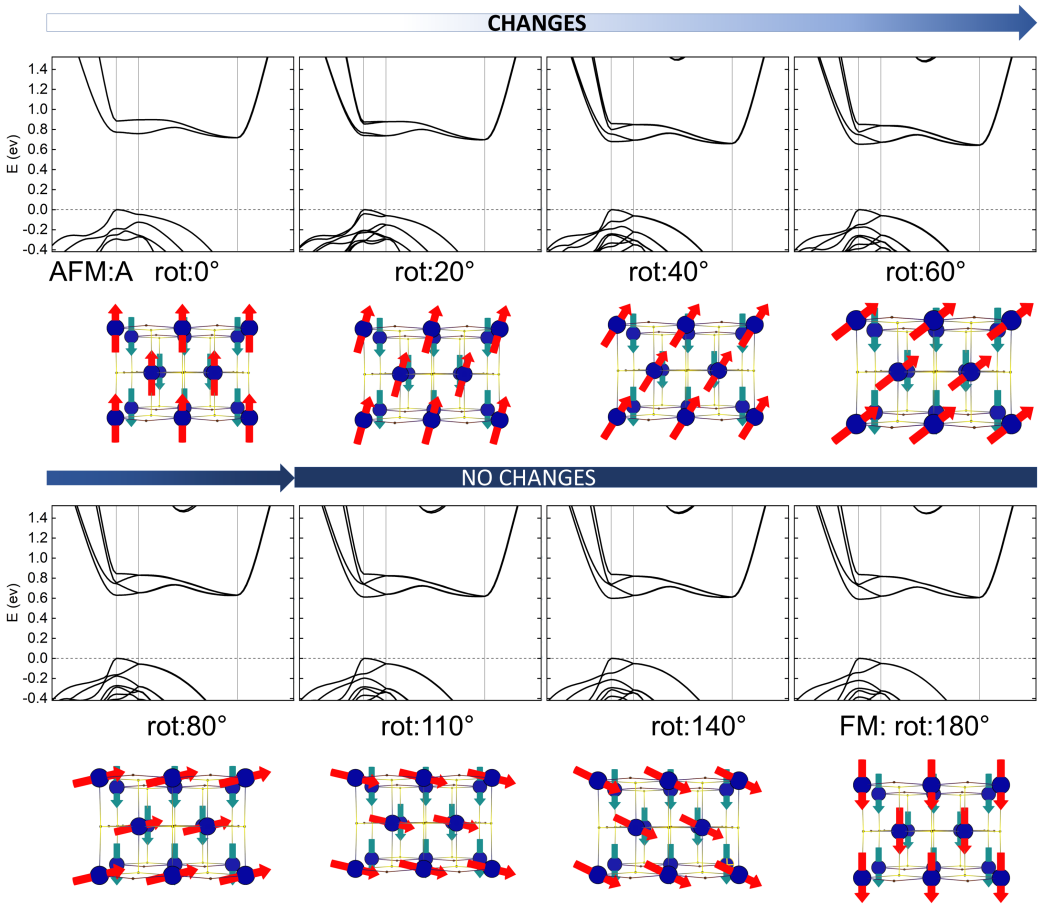

Fig. S10 (Color online) Band splitting around the Γ point upon rotation of the spins within one layer (red arrows) with respect to the fixed alignment of the spins in the adjacent layer (green arrows) as represented by the schematic diagrams below (perspective top view). The particular angle rot:20 indicates the angle between the spins coming from the nearest-neighbour atoms from adjacent layers.

5 Phonons

Positions of specific phonon modes are presented in Table 1

Table 1 Positions of specific phonon modes for calculations and Raman spectroscopy [cm^{-1}].

	AFM	FM	exp
$\mathbf{B}^1_{3g}$	74	73	
$\mathbf{B}^1_{2g}$	75	90	82
$\mathbf{B}^1_{2u}$	86	85	
$\mathbf{A}^1_{g}$	115	119	109
$\mathbf{B}^1_{3u}$	168	167	
$\mathbf{B}^2_{3g}$	170	188	184
$\mathbf{B}^2_{2g}$	171	184	188
$\mathbf{B}^1_{1u}$	212	211	
$\mathbf{A}^2_{g}$	238	239	243
$\mathbf{B}^2_{3u}$	284	299	
$\mathbf{B}^3_{2g}$	290	291	294
$\mathbf{A}^2_{g}$	331	329	336
$\mathbf{B}^2_{2u}$	342	317	
$\mathbf{B}^2_{1u}$	343	338	
$\mathbf{B}^3_{3g}$	363	354	357

Calculated phonon dispersion for two magnetic states and the temperature curves for (A^3_g) mode are shown of Fig. S11

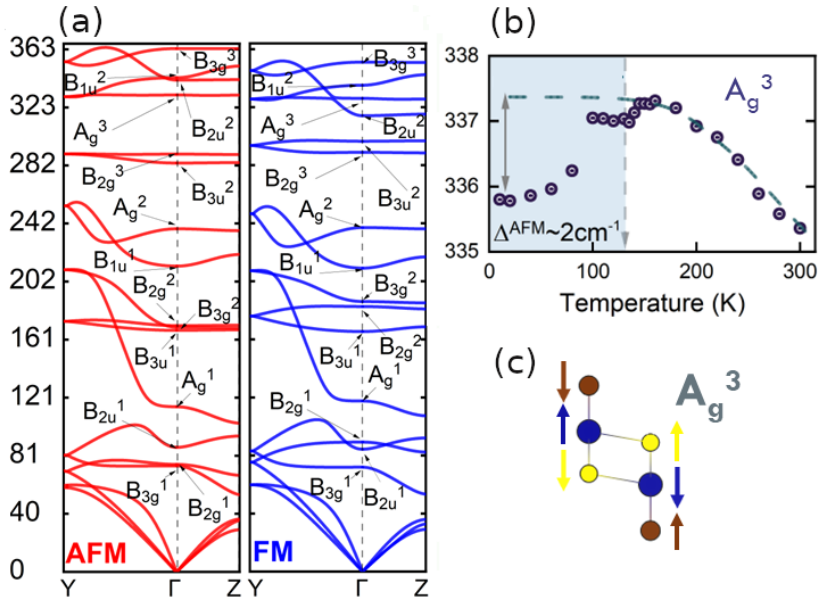

Fig. S11 (Color online) (a) Calculated phonon dispersion for two magnetic states, zoom in the vicinity of the Γ point. (b) Temperature curves for out-of-plane (A^3_g) mode and (c) its corresponding schematic representation.

References

1 O. Göser, W. Paul and H. Kahle, *Journal of Magnetism and Magnetic Materials*, 1990, **92**, 129–136.

2 E. J. Telford, A. H. Dismukes, K. Lee, M. Cheng, A. Wieteska, A. K. Bartholomew, Y.-S. Chen, X. Xu, A. N. Pasupathy, X. Zhu, C. R. Dean and X. Roy, *Advanced Materials*, 2020, **32**, 2003240.

3 E. J. Telford, A. H. Dismukes, R. L. Dudley, R. A. Wiscons, K. Lee, D. G. Chica, M. E. Ziebel, M.-G. Han, J. Yu, S. Shabani, A. Scheie, K. Watanabe, T. Taniguchi, D. Xiao, Y. Zhu, A. N. Pasupathy, C. Nuckolls, X. Zhu, C. R. Dean and X. Roy, *Nature Materials*, 2022, **21**, 754–760.